

Layered reduced graphene oxide with nanoscale interlayer gaps as a stable host for lithium metal anodes

Dingchang Lin^{1†}, Yayuan Liu^{1†}, Zheng Liang¹, Hyun-Wook Lee¹, Jie Sun¹, Haotian Wang², Kai Yan¹, Jin Xie¹ and Yi Cui^{1,3*}

Metallic lithium is a promising anode candidate for future high-energy-density lithium batteries. It is a light-weight material, and has the highest theoretical capacity ($3,860 \text{ mAh g}^{-1}$) and the lowest electrochemical potential of all candidates. There are, however, at least three major hurdles before lithium metal anodes can become a viable technology: uneven and dendritic lithium deposition, unstable solid electrolyte interphase and almost infinite relative dimension change during cycling. Previous research has tackled the first two issues, but the last is still mostly unsolved. Here we report a composite lithium metal anode that exhibits low dimension variation (~20%) during cycling and good mechanical flexibility. The anode is composed of 7 wt% 'lithophilic' layered reduced graphene oxide with nanoscale gaps that can host metallic lithium. The anode retains up to $\sim 3,390 \text{ mAh g}^{-1}$ of capacity, exhibits low overpotential (~80 mV at 3 mA cm^{-2}) and a flat voltage profile in a carbonate electrolyte. A full-cell battery with a LiCoO_2 cathode shows good rate capability and flat voltage profiles.

Lithium metal is the ultimate anode for Li batteries^{1–3}, but dendritic deposition and the infinite relative dimension change during cycling severely impede its practical applications^{4–8}. To realize Li metal anodes, continuous effort has been made for decades to understand the mechanism of Li deposition and tackle dendrite formation, as well as unstable solid electrolyte interphase (SEI)^{5,9–15}. The strategies employed previously can be broadly divided into three categories: (i) developing electrolyte additives for the stabilization of SEI^{16–21}; (ii) engineering high-modulus solid electrolytes to prevent dendrite penetration^{22–27}; and (iii) designing electrochemically and mechanically stable artificial interfaces for SEI stabilization and dendrite suppression^{28,29}. All of the above are efficacious to a certain extent for mitigating either or both dendritic Li growth and SEI collapse. Nevertheless, none of them is capable of addressing the infinite relative electrode dimension change caused by the 'hostless' Li plating/stripping. The stabilization of the electrode dimension is recognized to be equally important for practical applications of Li anodes. With infinite relative volume change, the resulting huge internal stress fluctuations and the floating interface can damage the cells, leading to potential safety hazards and causing tremendous engineering challenges for implementing the battery in a confined space. More importantly, SEI stability is also strongly correlated with dimension stability. The SEI may not be able to accommodate the drastic volume variation and would thus face the danger of collapse during continuous cycling^{7,8}. Such SEI collapse can in turn exacerbate the locally favourable Li dendrite growth and the continuous electrolyte decomposition. As a consequence, a new approach capable of solving these multifaceted problems would be indispensable.

The infinite dimension change of Li is originated from its 'hostless' nature. To address the problem, rational design of a 'host' for metallic Li is necessary. Carbon-based materials are the ideal host candidates

for Li metal. Carbon is among the lightest materials available for scaffold construction and emerging carbon materials such as carbon nanotubes^{30,31}, graphene^{32,33} and mesoporous carbon³⁴ have appealingly high surface areas with excellent mechanical strength. Moreover, carbon materials are generally stable under the redox environment in Li batteries. In previous Li-ion battery designs, the abovementioned advantages of carbon materials have therefore made them a great success as electrode materials and conducting additives^{35–44}.

In designing Li metal anodes it is important to pre-store Li into the electrode, which not only predefines the anode space, but also supplies the Li source—especially for high-energy-density battery systems such as $\text{Li}-\text{O}_2$ and $\text{Li}-\text{S}^4$. However, methods other than

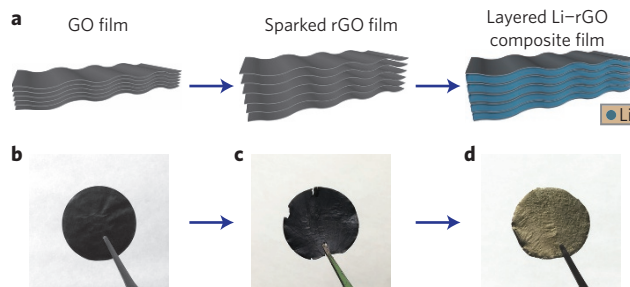


Figure 1 | Fabrication of a layered Li-rGO composite film. **a**, Schematic of the material design and the consequent synthetic procedures from a GO film (left) to a sparked rGO film (middle) to a layered Li-rGO composite film (right). **b–d**, Corresponding digital camera images of the GO film (**b**), sparked rGO film (**c**) and layered Li-rGO composite film (**d**). The diameters of the films shown in **b–d** are $\sim 47 \text{ mm}$.

¹Department of Materials Science and Engineering, Stanford University, Stanford, California 94305, USA. ²Department of Applied Physics, Stanford University, Stanford, California 94305, USA. ³Stanford Institute for Materials and Energy Sciences, SLAC National Accelerator Laboratory, 2575 Sand Hill Road, Menlo Park, California 94025, USA. [†]These authors contributed equally to this work. *e-mail: yicui@stanford.edu

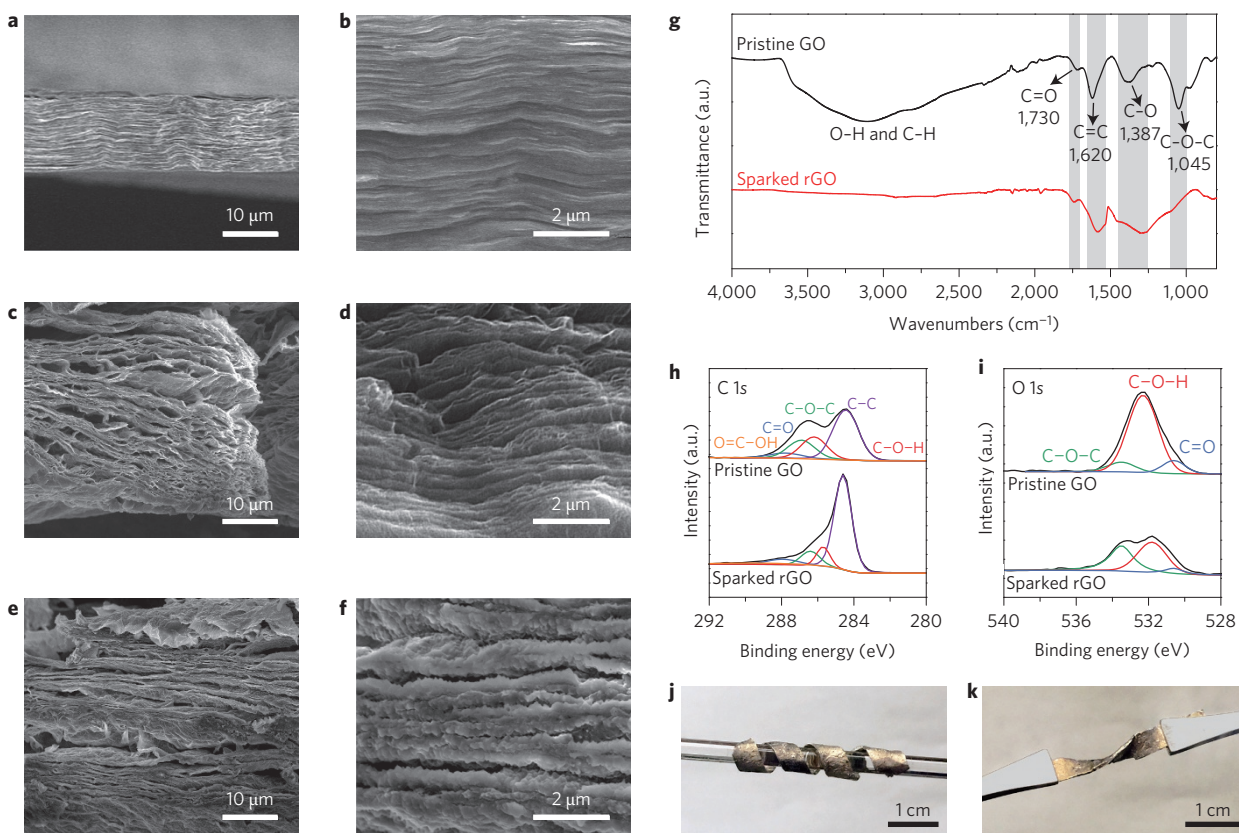


Figure 2 | Characterization of the materials. **a,b**, Low-magnification (**a**) and magnified (**b**) SEM images of the pristine GO film prepared by vacuum filtration. **c–f**, The corresponding SEM images of sparked rGO films (**c,d**) and layered Li-rGO films (**e,f**) are shown for comparison. **g**, FTIR spectra of a pristine GO film and a sparked rGO film. **h,i**, Deconvoluted XPS spectra of C 1s (**h**) and O 1s (**i**) before and after the spark reaction. **j**, A layered Li-rGO strip is coiled around a glass rod to illustrate the good flexibility. **k**, A layered Li-rGO strip is twisted by two tweezers to show the twistability.

electrodeposition are required, as this usually causes uneven Li distribution and inefficient fabrication. We found that thermal infusion is a prominent approach and to successfully infuse molten Li, the host needs to possess good Li affinity (lithiophilicity). Good lithiophilicity indicates a strong binding between Li and the materials' surface, which is critical for achieving both uniform molten Li infusion during synthesis and a low Li nucleation barrier in battery cycling. For most of the carbon materials, their relatively weak binding with Li leads to poor lithiophilicity, excluding many candidates as host materials. Reduced graphene oxide (rGO), however, exhibits high lithiophilicity, unique among all of the carbon-based materials.

Here we report a layered Li-rGO electrode made via molten Li infusion into an rGO film with uniform nanogaps. The electrode exhibits uniform periodic stacking of nanoscale layered Li and rGO. This structure has several notable advantages. First, layered rGO offers a stable scaffold for Li stripping/plating, which significantly mitigates the volume change at the electrode level during cycling. Second, the excellent lithiophilicity of rGO with a large surface area guarantees uniform Li infusion and deposition during synthesis and later cycling, respectively. Third, the top rGO cap layer provides an electrochemically and mechanically stable artificial interface that plays a role in stabilizing the as-formed SEI²⁹. Owing to these merits, layered Li-rGO films enabled highly improved electrochemical performances.

Fabrication of layered Li-rGO electrodes

Fabricating layered rGO films with uniform nanogaps and infusing Li into the interlayer gaps are two key steps for electrode fabrication (Fig. 1a). With densely stacked GO films as the starting material

(Fig. 1b)⁴⁵, we first developed a simple yet subtle 'spark' reaction for producing uniform nanogaps (Fig. 1a, step 1). When the GO film was partially put into contact with molten Li, a spark reaction can happen immediately across the whole film (Supplementary Movie 1), expanding the film into a much more porous structure. This phenomenon could be explained by the sudden pressure release within the GO layers due to the removal of superheated residual water/surface functional groups^{46,47} and the instant combustion of hydrogen formed under the reduction condition (Supplementary Fig. 1). The spark reaction successfully generated the desired nanogaps for Li deposition and partially reduced the GO film to selectively remove the reactive surface functional groups. As a consequence, a much more porous and stable scaffold can be obtained for Li intake and electrochemical cycling (Fig. 2c).

The other key step is to homogeneously infuse Li into the interlayer spacing (Fig. 1a, step 2). As shown in Supplementary Figure 2 and Supplementary Movie 2, fast and uniform Li intake can be fulfilled by simply bringing the edge of the rGO films into contact with molten Li. Less than 1 min is required for silvery Li to spread across the whole rGO film (Fig. 1d), unique among carbon materials (Supplementary Fig. 3). This distinct property is believed to be due to the synergistic effects of the lithiophilic nature of sparked rGO and the capillary force produced by the nanogaps. According to first-principles calculations (Supplementary Fig. 4), rGO surface groups such as carbonyl (3.080 eV) and alkoxy (2.974 eV) groups exhibit much stronger binding energy to Li than the bare graphene counterpart (1.983 eV). The strong binding can greatly increase the surface lithiophilicity for efficient Li intake. The capillary force is another critical factor for Li infusion (Supplementary Fig. 5). With a superior lithiophilic surface, capillary force can lift molten Li into rGO

interlayers. As reduced gap dimensions can provide a stronger capillary force, the nanoscale interlayer spacing here enabled a powerful driving force for fast Li intake.

Compared with the electrodeposition approach, pre-storing Li via thermal infusion has several distinguished advantages: no sacrificing cells are needed, which is practical for scalable production; the highly reactive molten Li removes unstable species at low potential of Li^+/Li , preventing continuous Li consumption in electrochemical cycling; and a uniform Li distribution can be easily obtained by thermal infusion, whereas electroplating usually brings about uneven Li deposition.

Characterizations of the materials

Figure 2a,b shows the low-magnification and magnified scanning electron microscope (SEM) images of the pristine GO film, which exhibited the typical densely stacked structure⁴⁵. After the spark reaction (Fig. 2c,d), significantly enlarged interlayer spacing can be clearly observed with uniform gaps of several hundred nanometres (Fig. 2d). Nitrogen sorption analysis (Supplementary Fig. 6) confirmed the increased porosity after the spark reaction, where the Brunauer–Emmett–Teller (BET) surface area of the film increased from merely $8.0 \text{ m}^2 \text{ g}^{-1}$ to $394.3 \text{ m}^2 \text{ g}^{-1}$. Once Li was infused into the rGO, as indicated in Fig. 2e,f, the nanogaps were filled by Li and the uniform layered structure was still maintained.

The selective reduction of the GO films by the spark reaction is supported by Fourier transform infrared spectroscopy (FTIR, Fig. 2g)⁴⁸, and X-ray photoelectron spectroscopy (XPS, Fig. 2h,i and Supplementary Fig. 7)⁴⁹. As shown in Fig. 2g, before the spark reaction, a strong peak corresponding to –OH stretching (broad peak beyond $3,000 \text{ cm}^{-1}$) was detected, which revealed the presence of a large proportion of –OH groups either in the form of adsorbed water or surface –OH. Simultaneously, characteristic peaks of other surface groups such as carbonyl ($\text{C}=\text{O}$) ($\sim 1,730 \text{ cm}^{-1}$) and epoxy ($\text{C}-\text{O}-\text{C}$) ($\sim 1,045 \text{ cm}^{-1}$) were also observed. In contrast, after the spark reaction the –OH peak became almost undetectable, confirming the removal of both residual water and surface –OH groups. However, despite a slight shift, the peaks of the other more stable oxygen-containing surface moieties were retained. Consistent with the FTIR result, the XPS spectra indicated a significant reduction in O after the spark reaction (Supplementary Fig. 8). And as can be observed from the deconvoluted C 1s and O 1s spectra (Fig. 2h,i), the intensity corresponding to $\text{C}-\text{O}-\text{H}$ dropped to $\sim 50\%$ of the original value, whereas the other surface functional groups exhibited limited decrease, confirming the selective removal of –OH groups. The Raman spectroscopy and X-ray diffraction patterns (Supplementary Figs 9 and 10) further confirmed the characteristic peaks of GO and rGO.

Good electrode flexibility is critical in battery manufacturing as both pouch and cylindrical cell configurations require flexibility for either folding or rolling processes. Thanks to the flexible nature of rGO and the layered structure, which minimized the built-in strain after folding, the layered Li-rGO exhibited good flexibility and twistability as shown in Fig. 2j,k and Supplementary Movie 3. Furthermore, by simply changing the thickness of the initial GO film, the thickness of the resulting electrode can be easily tuned (Supplementary Fig. 11), illustrating the suitability of our proposed method for real world applications.

SEM and *in situ* TEM characterizations of Li plating/stripping

Using a carbonate-based electrolyte in Li metal batteries is challenging due to its relatively positive reduction potential and the brittleness of the SEI layer⁵⁰. However, it is important to study Li metal in a carbonate environment as the flammability is lower than for ether electrolytes and the carbonate environment is more compatible with industrial techniques. In this work, a carbonate-based electrolyte was used to conduct our experiments.

Figure 3a–c shows the cross-section SEM images of pristine Li-rGO, the film after Li stripping and after one stripping/plating cycle, respectively. When Li was stripped (Fig. 3b), the interlayered gaps originally occupied by metallic Li appeared again. This illustrates that the interlayered spacing did not undergo obvious changes during the initial infusion and later stripping steps. After plating Li back (Fig. 3c), most of the interlayered spacing was refilled by Li. Although the deposited Li exhibited a different morphology compared with the initial stage, no obvious dendritic Li can be observed. The surface morphology after multiple cycles was also characterized in comparison with the bare Li foil counterpart (Fig. 3d–i). After 10 cycles, the Li foil exhibited a mossy, dendritic Li deposition (Fig. 3d,e), whereas the layered Li-rGO surface remained smooth without observable dendrites (Fig. 3f,g). The uniform deposition can be sustained even at 3 mA cm^{-2} (Fig. 3h, i) and 5 mA cm^{-2} (Supplementary Fig. 12), where the cycled electrodes still maintained flat and clean surface. After 100 cycles, the surface with SEI coverage still exhibited a relatively smooth and dense morphology (Supplementary Fig. 13a). No obvious step can be observed at the SEI boundary (Supplementary Fig. 13b), indicating a relatively thin SEI layer. On the surface with SEI removed (Supplementary Fig. 13c), Li deposited under the rGO sheets. The evidence indicates that even for a longer cycle, Li can still be successfully deposited back into the layered rGO matrix.

To visualize the Li deposition behaviour, *in situ* transmission electron microscopy (TEM) was exploited using a specialized dual-probe biasing TEM holder. The *in situ* TEM device is schematically illustrated in Fig. 3j. Both side-view (Fig. 3k) and top-view (Fig. 3l) characterizations were carried out to obtain comprehensive information on Li deposition (Supplementary Movies 4 and 5). From the time-evolution side-view images, only a minimal thickness change can be observed after Li deposition (Fig. 3k), showing the merit of a layered rGO host for dimension stabilization. The injection of Li into the interlayered rGO spacing was confirmed by electron energy loss spectroscopy (EELS, Fig. 3m), measurements were made at the interlayer spots marked in Fig. 3k, where characteristic Li peaks appeared after Li deposition. In contrast, when Li was deposited onto a substrate without a host, dendritic Li can shoot out on the surface (Supplementary Fig. 14 and Movie 6). The relatively stable dimension can be further confirmed by the *ex situ* SEM study after Li stripping and plating, which showed only a $\sim 20\%$ thickness fluctuation (Supplementary Fig. 15). The top-view characterization consolidates the Li confinement in the stable host. As shown in Fig. 3l and Supplementary Movie 5, the rGO sheet showed Li infusion with slightly expanded lateral dimensions. The even expansion across the whole rGO sheet illustrates better Li plating behaviour.

The observed uniform Li deposition can be rationalized by the highly increased nucleation sites and the nearly full interfacial protection by the rGO layers. The large number of two-dimensional Li interlayers greatly enhanced the activated surface area for Li deposition. As a minimal energy barrier is required to deposit Li directly on Li, much more uniform Li nucleation on the large Li surface in the layers can be achieved. In addition, the flexible and mechanically strong rGO layer acts as the stable artificial interface. It was reported that graphene cap layers are capable of maintaining stable SEI and accommodating dimension fluctuation²⁹. Here, with the stable rGO at the interface and the small dimension change, SEI cracking and the resulting ‘hot spots’ for uneven Li deposition can be highly suppressed.

Electrochemical testing of layered Li-rGO anodes

Figure 4a compares the voltage profiles of symmetric layered Li-rGO electrode cells and the bare Li foil counterparts through over 100 cycles at 1 mA cm^{-2} . Li-rGO exhibited stable voltage profiles with small hysteresis, whereas the Li foils displayed a gradual

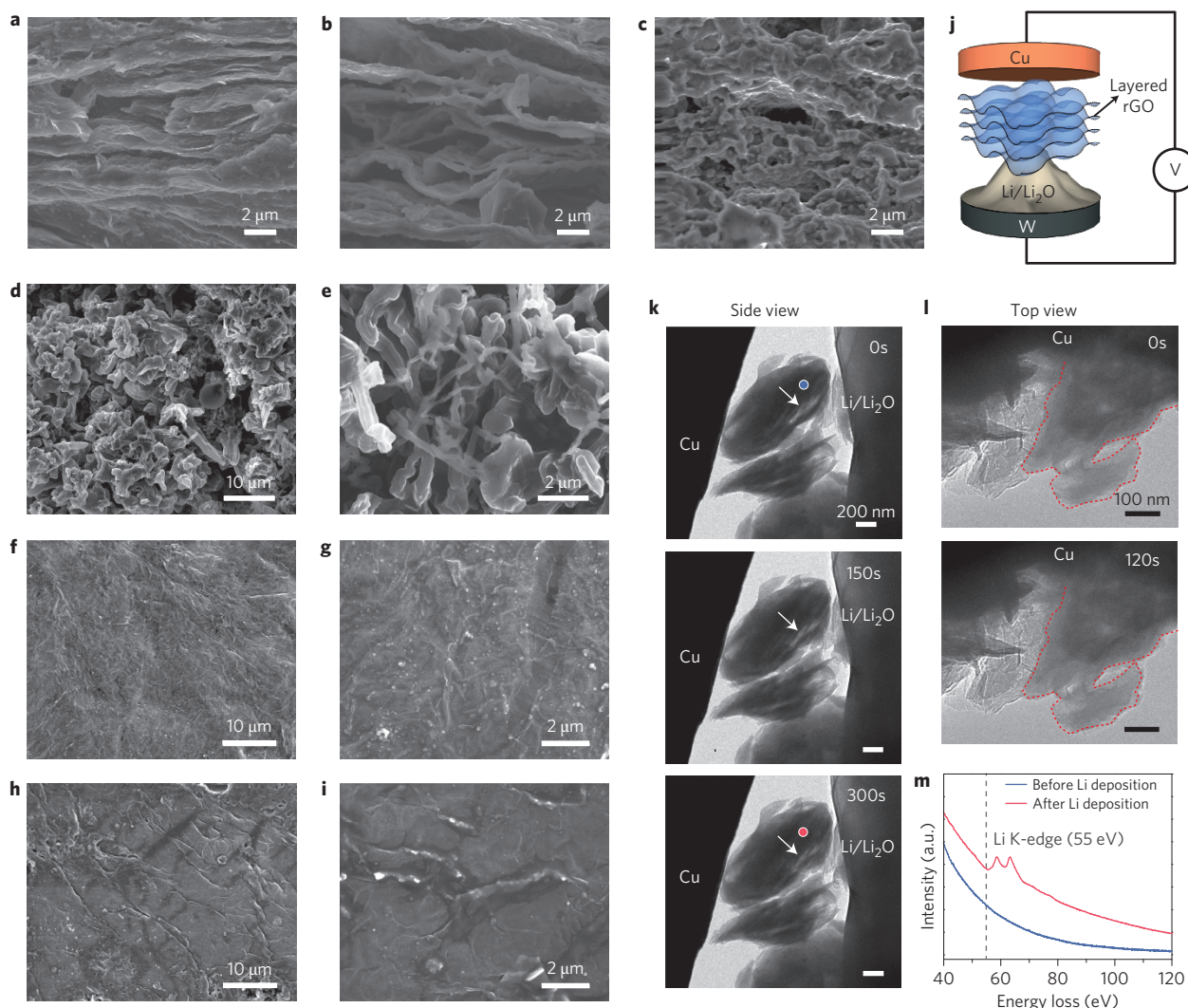


Figure 3 | Li deposition behaviour and *in situ* characterization. **a–c**, Cross-section SEM images of the Li-rGO electrode before (**a**) and after (**b**) Li stripping, and after 1 stripping/plating cycle (**c**). **d,e**, SEM images of the bare Li foil surface after 10 galvanostatic cycles. **f,g**, SEM images of the Li-rGO surface after 10 galvanostatic cycles. The current density of the cells shown in **d–g** was fixed at 1 mA cm^{-2} whereas the capacity was set at 1 mAh cm^{-2} . **h,i**, SEM image of the Li-rGO electrode surface after 10 galvanostatic cycles with a higher current density of 3 mA cm^{-2} . **j**, Schematic of the *in situ* TEM cell configuration. **k**, Time-lapse images showing the side view of an rGO film during the Li deposition process (Supplementary Movie 4). **l**, Top view of an rGO film at the initial (top) and final (bottom) stages of Li deposition (Supplementary Movie 5). **m**, EELS spectra of an rGO film before and after Li deposition. The signals were collected at the positions marked in **k** at the initial (blue dot) and final (red dot) stages, respectively.

increase in hysteresis over cycles, by almost 100% after 100 cycles. To study the evolution of the voltage profiles in detail, the 1st, 10th, 50th and 100th cycle of the layered Li-rGO cells were further enlarged as the insets in Fig. 4a. For layered Li-rGO, flat voltage plateaus at both the charging and discharging states can be retained throughout the whole cycle without obvious increases in hysteresis. This is a significant improvement compared with bare Li electrodes, which showed fluctuating voltage profiles with consistently higher overpotential at both the initial and final stages of each stripping/plating process (Supplementary Fig. 16). Beyond 100 cycles (250 cycles), as shown in Supplementary Fig. 17, the layered Li-rGO still exhibited outstanding cycling stability and constantly low hysteresis. In an ether-based electrolyte, the layered Li-rGO exhibited even better cycling stability (Supplementary Fig. 18).

At an increased current density of 2 mA cm^{-2} (Supplementary Fig. 19) and 3 mA cm^{-2} (Fig. 4b), stable cycling beyond 100 cycles with stable hysteresis can still be attained, whereas the Li foil counterparts exhibited gradual hysteresis augment. After 92 cycles

(Fig. 4b), a sudden voltage drop was detected for the Li foils with fluctuating voltage in the later cycles, which could be explained by an internal soft short-circuit with Li dendrite penetration. The enlarged voltage profiles of the selected cycles shown in Fig. 4b further confirm the stable cycling of Li-rGO with flat voltage plateaus through the cycles. When the cycling capacity was increased to 3 mAh cm^{-2} , the layered Li-rGO still exhibited much improved performance (Supplementary Fig. 20). Only a slight increase in hysteresis was observed for the layered Li-rGO, whereas Li foils showed significant hysteresis increases even in the early cycles.

The highly reduced polarization and stable cycling can be further supported by the electrochemical impedance spectroscopy (EIS) analysis conducted on symmetric cells before cycling (Supplementary Fig. 21) and after 10 cycles (Fig. 4c). The corresponding Nyquist plots are shown; the semicircle at the high-frequency range is a good indicator of the interfacial resistance at SEI and the charge transfer resistance at the Li surface⁸. The Li foils showed an extremely large interfacial resistance of $\sim 650\ \Omega$

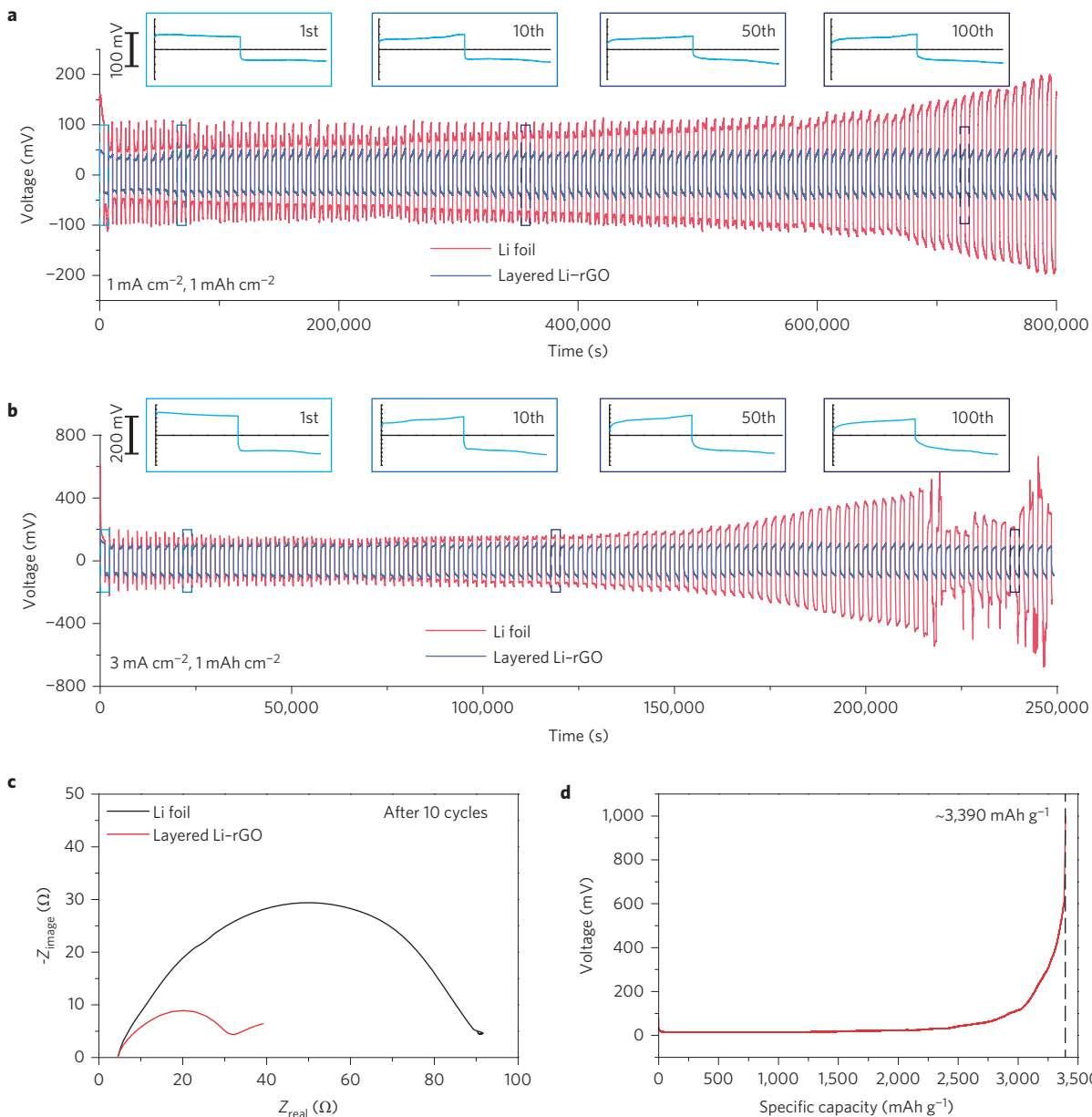


Figure 4 | Electrochemical characterization of the Li-rGO electrodes. **a**, Galvanostatic cycling of a symmetric Li-rGO electrode (blue) and bare Li foil (red) in the first 800,000 s. The current density was fixed at 1 mA cm⁻² with a stripping/plating capacity of 1 mAh cm⁻². Insets, detailed voltage profiles of the 1st, 10th, 50th and 100th cycles, respectively. The y axis scale of the insets is shown on the left. **b**, Corresponding higher current density (3 mA cm⁻²) cycling of a symmetric Li-rGO electrode (blue) and bare Li foil (red) in the first 250,000 s. Insets, detailed voltage profiles, with cycle numbers indicated. **c**, Nyquist plots of the symmetric cells after 10 galvanostatic cycles. **d**, Full Li stripping curve of the Li-rGO electrode to 1 V versus Li⁺/Li, which shows a specific capacity of $\sim 3,390 \text{ mAh g}^{-1}$.

before cycling, which originates from the native oxide layers formed on the electrodes. After 10 cycles, interfacial resistance dropped to a much lower value of $\sim 85 \Omega$ due to the collapse of the native oxide layers and the dendritic Li formation, which significantly increased the surface area. In contrast, the layered Li-rGO had constantly low interfacial resistance of $\sim 30 \Omega$ before cycling and $\sim 25 \Omega$ after 10 cycles. This phenomenon illustrates that much better electrode stability and more favourable Li stripping/plating kinetics can be achieved with layered Li-rGO.

Notably, layered Li-rGO not only exhibited outstanding electrochemical properties, but also retained most of the capacity. As shown in Fig. 4d, a capacity of $\sim 3,390 \text{ mAh g}^{-1}$ (based on the weight of the whole electrode) can be extracted when charged to 1 V, which is very close to the theoretical capacity of pure Li

($\sim 87.8\%$ capacity retention compared with pure Li). The high specific capacity can be attributed to the light-weight and porous nature of sparked rGO where the mass of the framework only took up ~ 7 wt% of the whole electrode. Therefore, the specific choice of the carbon-based host material offers the exciting possibility of fabricating high-performance Li anodes with a minimal effect on capacity.

In cells paired with lithium cobalt oxide (LiCoO₂, LCO) (Fig. 5 and Supplementary Fig. 22) and lithium titanium oxide (Li₄Ti₅O₁₂, LTO) (Supplementary Fig. 23), the layered Li-rGO anodes consistently exhibited a much better rate capability and lower hysteresis. As shown in Fig. 5a, with Li-rGO anodes, a much higher LCO capacity can be retained especially at a high rate ($\sim 110 \text{ mAh g}^{-1}$ at 4 C and $\sim 70 \text{ mAh g}^{-1}$ at 10 C; x C = fully

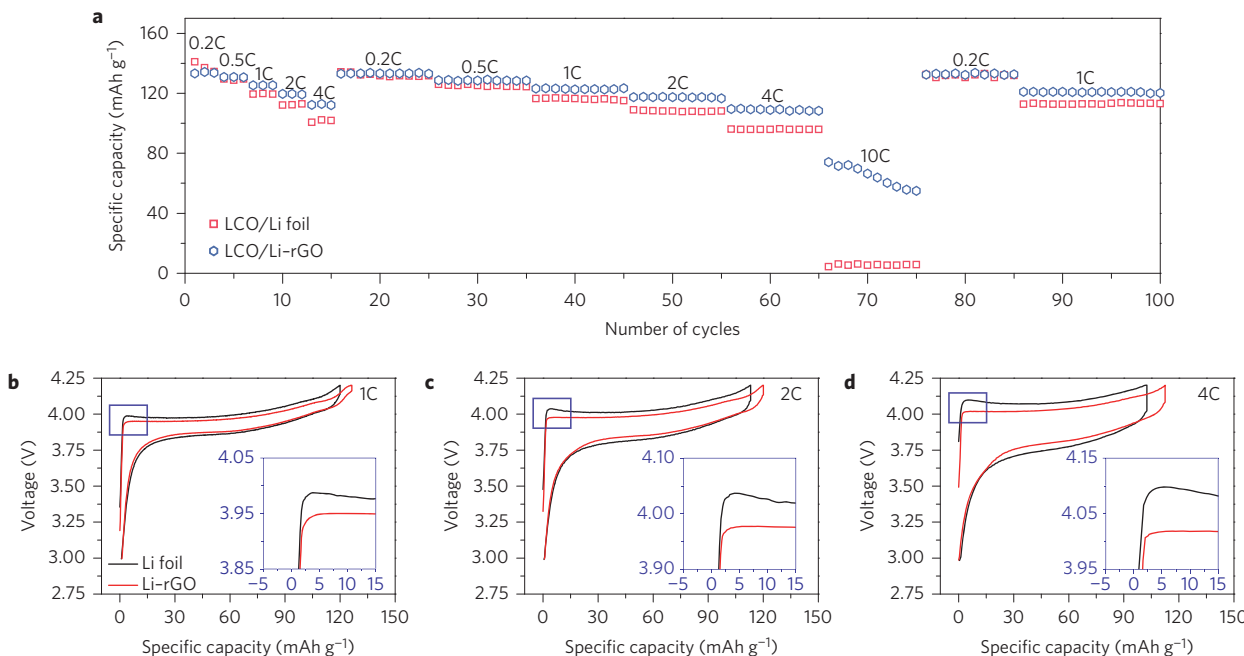


Figure 5 | Electrochemical performance of the LCO/Li-rGO cells. **a**, Rate capability of the LCO/Li-rGO and LCO/Li foil cells at various rates from 0.2 C to 10 C. **b–d**, Voltage profile comparison of the LCO/Li-rGO cells and the LCO/Li foil cells at rates of 1 C (**b**), 2 C (**c**) and 4 C (**d**). The detailed overpotential profiles at the initial charge stages (blue squares) were enlarged and shown as insets in **b–d**.

discharge within 1/x hours). In contrast, Li foil cells only offer ~ 95 mAh g⁻¹ and ~ 5 mAh g⁻¹ at 4 C and 10 C, respectively. The comparison of the voltage profiles at different rates confirms a much more stable Li metal anode with lower overpotential and flat voltage plateaus. It can be seen that different from the layered Li-rGO cells, Li foil cells consistently show higher overpotential at the initial stage of charging leading to a ‘bump’ shape as marked and enlarged in Fig. 5b–d, which is more significant at increased rates. This is consistent with the symmetric Li foil cycling where bumps show at the initial and final stages of each plating/stripping process (Supplementary Fig. 16). This demonstrates the improved power and stability with layered Li-rGO.

Furthermore, we found that high-areal-capacity LTO can serve as an ideal Li reservoir to evaluate the Coulombic efficiency of an electrode with excess pre-stored Li (Supplementary Fig. 24). Here, ~ 10 mAh cm⁻² of Li electrodes were paired with ~ 3 mAh cm⁻² of LTO. The cell with layered Li-rGO exhibited much better cycling stability (for >65 cycles) than the bare Li foil (~ 14 cycles) and electrodeposited Li (~ 8 cycles), indicating reduced Li loss and thus higher Coulombic efficiency.

Conclusions

In this work, we designed a layered Li-rGO composite for use as a Li metal anode. The spark reaction of GO in contact with molten Li was performed to obtain a uniform layered nanostructure, and molten Li infusion was developed for pre-storing Li into the lithiophilic interlayer spacing of the sparked rGO. The anode exhibits excellent flexibility and a small electrode dimensional change ($\sim 20\%$) during cycling with stable SEI. These characteristics give rise to stable cycling with low hysteresis both in symmetric-cell and full-cell configurations even in a carbonate-based electrolyte. We believe that our design is a viable option for fabricating stable Li anodes for high-energy and high-power Li battery systems.

Methods

Methods and any associated references are available in the online version of the paper.

Received 15 October 2015; accepted 12 February 2015; published online 21 March 2016

References

- Tarascon, J. M. & Armand, M. Issues and challenges facing rechargeable lithium batteries. *Nature* **414**, 359–367 (2001).
- Armand, M. & Tarascon, J. M. Building better batteries. *Nature* **451**, 652–657 (2008).
- Chu, S. & Majumdar, A. Opportunities and challenges for a sustainable energy future. *Nature* **488**, 294–303 (2012).
- Bruce, P. G., Freunberger, S. A., Hardwick, L. J. & Tarascon, J. M. Li-O₂ and Li-S batteries with high energy storage. *Nature Mater.* **11**, 19–29 (2012).
- Xu, W. *et al.* Lithium metal anodes for rechargeable batteries. *Energy Environ. Sci.* **7**, 513–537 (2014).
- Yamaki, J.-i. *et al.* A consideration of the morphology of electrochemically deposited lithium in an organic electrolyte. *J. Power Sources* **74**, 219–227 (1998).
- Aurbach, D., Zinigrad, E., Cohen, Y. & Teller, H. A short review of failure mechanisms of lithium metal and lithiated graphite anodes in liquid electrolyte solutions. *Solid State Ionics* **148**, 405–416 (2002).
- Bieker, G., Winter, M. & Bieker, P. Electrochemical *in situ* investigations of SEI and dendrite formation on the lithium metal anode. *Phys. Chem. Chem. Phys.* **17**, 8670–8679 (2015).
- Peled, E. The electrochemical behavior of alkali and alkaline earth metals in nonaqueous battery systems—the solid electrolyte interphase model. *J. Electrochem. Soc.* **126**, 2047–2051 (1979).
- Aurbach, D. *et al.* Attempts to improve the behavior of Li electrodes in rechargeable lithium batteries. *J. Electrochem. Soc.* **149**, A1267–A1277 (2002).
- Xu, K. Electrolytes and interphases in Li-ion batteries and beyond. *Chem. Rev.* **114**, 11503–11618 (2014).
- Bhattacharyya, R. *et al.* *In situ* NMR observation of the formation of metallic lithium microstructures in lithium batteries. *Nature Mater.* **9**, 504–510 (2010).
- Chandrashekhar, S. *et al.* ⁷Li MRI of Li batteries reveals location of microstructural lithium. *Nature Mater.* **11**, 311–315 (2012).
- Harry, K. J., Hallinan, D. T., Parkinson, D. Y., MacDowell, A. A. & Balsara, N. P. Detection of subsurface structures underneath dendrites formed on cycled lithium metal electrodes. *Nature Mater.* **13**, 69–73 (2014).
- Lu, Y., Tu, Z. & Archer, L. A. Stable lithium electrodeposition in liquid and nanoporous solid electrolytes. *Nature Mater.* **13**, 961–969 (2014).
- Ota, H., Shima, K., Ue, M. & Yamaki, J.-i. Effect of vinylene carbonate as additive to electrolyte for lithium metal anode. *Electrochim. Acta* **49**, 565–572 (2004).
- Ota, H., Sakata, Y., Wang, X., Sasahara, J. & Yasukawa, E. Characterization of lithium electrode in lithium imides/ethylene carbonate and cyclic ether electrolytes: II. surface chemistry. *J. Electrochem. Soc.* **151**, A437–A446 (2004).

18. Ding, F. *et al.* Dendrite-free lithium deposition via self-healing electrostatic shield mechanism. *J. Am. Chem. Soc.* **135**, 4450–4456 (2013).
19. Qian, J. *et al.* High rate and stable cycling of lithium metal anode. *Nature Commun.* **6**, 6362 (2015).
20. Crowther, O. & West, A. C. Effect of electrolyte composition on lithium dendrite growth. *J. Electrochem. Soc.* **155**, A806–A811 (2008).
21. Li, W. *et al.* The synergistic effect of lithium polysulfide and lithium nitrate to prevent lithium dendrite growth. *Nature Commun.* **6**, 7436 (2015).
22. Stone, G. M. *et al.* Resolution of the modulus versus adhesion dilemma in solid polymer electrolytes for rechargeable lithium metal batteries. *J. Electrochem. Soc.* **159**, A222–A227 (2012).
23. Bouchet, R. *et al.* Single-ion BAB triblock copolymers as highly efficient electrolytes for lithium-metal batteries. *Nature Mater.* **12**, 452–457 (2013).
24. Bates, J. B., Dudney, N. J., Neudecker, B., Ueda, A. & Evans, C. D. Thin-film lithium and lithium-ion batteries. *Solid State Ionics* **135**, 33–45 (2000).
25. Kanno, R. & Murayama, M. Lithium ionic conductor thio-LISICON: the $\text{Li}_2\text{SGeS}_2\text{P}_2\text{S}_5$ system. *J. Electrochem. Soc.* **148**, A742–A746 (2001).
26. Kamaya, N. *et al.* A lithium superionic conductor. *Nature Mater.* **10**, 682–686 (2011).
27. Murugan, R., Thangadurai, V. & Weppner, W. Fast lithium ion conduction in garnet-type $\text{Li}_2\text{La}_3\text{Zr}_2\text{O}_{12}$. *Angew. Chem. Int. Ed.* **46**, 7778–7781 (2007).
28. Zheng, G. *et al.* Interconnected hollow carbon nanospheres for stable lithium metal anodes. *Nature Nanotech.* **9**, 618–623 (2014).
29. Yan, K. *et al.* Ultrathin two-dimensional atomic crystals as stable interfacial layer for improvement of lithium metal anode. *Nano Lett.* **14**, 6016–6022 (2014).
30. Iijima, S. & Ichihashi, T. Single-shell carbon nanotubes of 1-nm diameter. *Nature* **363**, 603–605 (1993).
31. Yu, M.-F. *et al.* Strength and breaking mechanism of multiwalled carbon nanotubes under tensile load. *Science* **287**, 637–640 (2000).
32. Novoselov, K. S. *et al.* Two-dimensional gas of massless Dirac fermions in graphene. *Nature* **438**, 197–200 (2005).
33. Geim, A. K. & Novoselov, K. S. The rise of graphene. *Nature Mater.* **6**, 183–191 (2007).
34. Ying, J. Y., Mehnert, C. P. & Wong, M. S. Synthesis and applications of supramolecular-templated mesoporous materials. *Angew. Chem. Int. Ed.* **38**, 56–77 (1999).
35. Dahn, J. R., Zheng, T., Liu, Y. H. & Xue, J. S. Mechanisms for lithium insertion in carbonaceous materials. *Science* **270**, 590–593 (1995).
36. Ng, S. H., Wang, J., Guo, Z. P., Wang, G. X. & Liu, H. K. Single wall carbon nanotube paper as anode for lithium-ion battery. *Electrochim. Acta* **51**, 23–28 (2005).
37. Lee, S. W. *et al.* High-power lithium batteries from functionalized carbon-nanotube electrodes. *Nature Nanotech.* **5**, 531–537 (2010).
38. Hu, L. B. *et al.* Silicon-carbon nanotube coaxial sponge as Li-ion anodes with high areal capacity. *Adv. Energy Mater.* **1**, 523–527 (2011).
39. Wang, H. L. *et al.* Graphene-wrapped sulfur particles as a rechargeable lithium-sulfur battery cathode material with high capacity and cycling stability. *Nano Lett.* **11**, 2644–2647 (2011).
40. Liu, J. Charging graphene for energy. *Nature Nanotech.* **9**, 739–741 (2014).
41. Raccichini, R., Varzi, A., Passerini, S. & Scrosati, B. The role of graphene for electrochemical energy storage. *Nature Mater.* **14**, 271–279 (2015).
42. Son, I. H. *et al.* Silicon carbide-free graphene growth on silicon for lithium-ion battery with high volumetric energy density. *Nature Commun.* **6**, 7393 (2015).
43. Zhou, G., Paek, E., Hwang, G. S. & Manthiram, A. Long-life Li/polysulphide batteries with high sulphur loading enabled by lightweight three-dimensional nitrogen/sulphur-codoped graphene sponge. *Nature Commun.* **6**, 7760 (2015).
44. Reddy, A. L. M. *et al.* Synthesis of nitrogen-doped graphene films for lithium battery application. *ACS Nano* **4**, 6337–6342 (2010).
45. Dikin, D. A. *et al.* Preparation and characterization of graphene oxide paper. *Nature* **448**, 457–460 (2007).
46. Sun, G. *et al.* Actuation triggered exfoliation of graphene oxide at low temperature for electrochemical capacitor applications. *Carbon* **68**, 748–754 (2014).
47. Gao, Y. *et al.* Popping of graphite oxide: application in preparing metal nanoparticle catalysts. *Adv. Mater.* **27**, 4688–4694 (2015).
48. Marcano, D. C. *et al.* Improved synthesis of graphene oxide. *ACS Nano* **4**, 4806–4814 (2010).
49. Ganguly, A., Sharma, S., Papakonstantinou, P. & Hamilton, J. Probing the thermal deoxygenation of graphene oxide using high-resolution *in situ* X-ray-based spectroscopies. *J. Phys. Chem. C* **115**, 17009–17019 (2011).
50. Aurbach, D. *Nonaqueous Electrochemistry* (CRC, 1999).

Acknowledgements

Y.C. acknowledges the support from the Assistant Secretary for Energy Efficiency and Renewable Energy, Office of Vehicle Technologies of the US Department of Energy under the Battery Materials Research (BMR) program.

Author contributions

D.L., Y.L. and Y.C. conceived the idea and experiments. D.L. and Y.L. carried out the synthesis and performed the materials characterizations and electrochemical measurements. Z.L. assisted the electrochemical measurements. H.W.L. conducted *in situ* TEM characterization. J.S. performed the first-principles calculations. H.W. and K.Y. assisted in the Raman and XPS measurement. J.X. assisted the XPS analysis. D.L., Y.L. and Y.C. co-wrote the paper. All authors discussed the results and commented on the manuscript.

Additional information

Supplementary information is available in the online version of the paper. Reprints and permissions information is available online at www.nature.com/reprints. Correspondence and requests for materials should be addressed to Y.C.

Competing financial interests

The authors declare no competing financial interests.

Methods

Electrodes synthesis. Vacuum filtration with an anodic aluminum oxide membrane (AAO, Whatman, with diameter of ~47 mm and pore size of ~0.2 µm) as filter was used to yield the densely packed GO films. The highly concentrated GO solution (5 g l⁻¹, Graphene Supermarket) was commercially available and used as received. The as-obtained freestanding GO films were dried in a vacuum oven at 60 °C for 48 hours and then transferred to an argon-filled glove box with sub-ppm O₂ level. To perform the sparkle reaction, Li foils (99.9%, Alfa Aesar) were first melted in a stainless steel pan on a hot plate at ~250 °C. The GO films were then put into contact with the molten Li and the spark reaction occurs within seconds (as shown in Supplementary Movie 1). The spark reaction can partially reduce the GO films into rGO films. The rGO films were gently pressed between two stainless steel plates to obtain smooth surfaces. The edges of the pressed rGO films were brought into contact with the molten Li, which then infused into the rGO films with an observable colour change from black to silver (Supplementary Movie 2). The films can act as the electrodes once cooled down to room temperature.

Characterizations. An FEI XL30 Sirion scanning electron microscope is used for SEM characterization. Before conducting SEM studies of the cycled electrodes, the batteries were first disassembled in the glovebox and then gently rinsed in DOL to remove residue Li salts. XPS analysis was obtained on an SSI SProbe XPS spectrometer with an Al(Kα) source. Raman spectra were measured on a WITEC Raman spectrometer with a 531 nm excitation laser. FTIR spectra were recorded on a Nicolet iS50 FT-IR Spectrometer (Thermo Scientific). XRD patterns were recorded on a PANalytical X'Pert instrument and the Li-rGO electrode was loaded on a glass slide and covered with Kapton tape during measurements to avoid direct contact with air. N₂ sorption studies were performed in a Micromeritics ASAP 2020 adsorption apparatus at 77 K and at pressures up to 1 bar after the samples were first degassed at 180 °C overnight. The BET surface area was calculated using the adsorption data in a relative pressure ranging from 0.1 to 0.3.

In situ TEM observation. The *in situ* electrochemical experiment was carried out in an FEI Titan 80–300 environmental TEM at an acceleration voltage of 300 kV. A Nanofactory Instruments Dual-Probe STM-TEM *in situ* sample holder was used to demonstrate the lithiation process of rGO. A Cu metal wire with a sparked rGO film was employed as one electrode and a W wire covered by Li as the other. A thin oxide layer on the surface of the Li electrode acts as the solid electrolyte in the cell, and Li metal was used for the counter-electrode in the STM-TEM holder. As the Li metal electrode was transferred into the TEM, the electrode was exposed to air for about 5 s to create a layer of Li₂O about 20 nm thick, functioning as a solid electrolyte. A relative bias of -3.4 V was induced between the two electrodes, which caused Li⁺ ions to be transferred to the rGO electrode through the solid electrolyte. During the experiment the electron beam was widened to lessen electron beam effects.

Electrochemistry. To study the Li stripping/plating processes, the electrodes were assembled into 2032-type coin cells (MTI) in a symmetric cell configuration. The electrodes used here were either layered Li-rGO films or the freshly scraped Li foils (99.9%, Alfa Aesar). To prepare LCO and LTO electrodes for testing, the active materials (LCO and LTO powders from MTI) were mixed with polyvinylidene fluoride (PVDF, MTI) and carbon black (TIMCAL) at a ratio of 8:1:1 with *N*-Methyl-2-pyrrolidone (NMP) as the solvent. Electrodes with areal mass loading of ~2.5 mg cm⁻² were used for both LCO and LTO. For battery cycling with a limited amount of Li, LTO electrodes with areal capacities of ~3 mAh cm⁻² were used. The electrolytes employed were either 1M lithium hexafluorophosphate (LiPF₆) in 1:1 ethylene carbonate (EC)/diethyl carbonate (DEC) (BASF Selectlyte LP40) with 2% vinylene carbonate (VC) as the additive for carbonate-based system study (symmetric cells and LCO/LTO cells), or 1M Lithium bis(trifluoromethanesulphonyl)imide (LiTFSI) in 1:1 v/v 1,3-dioxolane (DOL)/1,2-dimethoxyethane (DME) with 1 wt% lithium nitrate for the ether-based system. Celgard 2325 (25 µm PP/PE/PP) was used as the separator. Galvanostatic cycling was conducted either on an Arbin 96-channel battery tester or a LAND 8-channel battery tester. The electrochemical impedance spectroscopy measurements were carried out on a Biologic VMP3 system.